CEOF Analysis of TOPEX and Model Sea Level Variations in the Arabian Sea

Sujit Basu[1] and Steven D. Meyers

Center for Ocean-Atmospheric Prediction Studies
The Florida State University
Tallahassee, FL 32306-2840

---

[1]Visiting from the Space Applications Centre (Indian Space Research Organization) in Ahmedabad, India.

COAPS Technical Report 97-5
October, 1997

Abstract.

Sealevel in the Arabian Sea is examined during 1993-94 using both a numerical reduced gravity model with realistic coastline geometry and windstress, and sealevel anomalies from the TOPEX altimeter. Differences between the model and altimetry arise due to the model's limited spatial domain and the lack of coastal currents (e.g., Somali Current) in this TOPEX dataset. These differences yield clues to the upper-layer dynamics in the Arabian Sea.

The annual cycle is shown to be composed of both propagating and non-propagating features. Some of the propagating features are found to be wind generated within the Arabian basin, some appear to originate in the Bay of Bengal, and some are generated by windstress along the northwest coast of India.

CEOF analysis isolates the annual cycle within the first mode, which is about 71% of the variance for the model and 58% of the variance for the altimetry data. The resulting spatial phase diagrams indicates regions of westward propagation in the model Arabian Sea north of 12°N, and north of the equator for the altimetry data.

1.INTRODUCTION

The Arabian Sea (AS) is characterized by seasonal changes of its surface circulation due to the two opposite northeast and southwest monsoon regimes. The Somali Current flows northeastward during the southwest monsoon and flows southwestward during the northeast monsoon. The seasonal variation of the wind-driven circulation pattern in this part of the Indian Ocean is greater than that in any other ocean. Previous modeling studies of this region have generally been concerned with the generation of the Somali Current and the gyres like the Great Whirl and the Southern Gyre during the onset of the summer monsoon [*Luther and O'Brien*, 1985; *McCreary and Kundu*, 1988; *Simmons et al.*, 1988; *Kindle and Thompson*, 1989]. In-situ observations of this ocean are confined to small regions [*Schott*, 1987], although there are studies describing the seasonal variations across the entire Indian Ocean [*Rao et al.*, 1989; *Molinari et al.*, 1990]. These are based on climatological observations. *Rao et al.* [1989] generated mean monthly mixed layer depth, sea surface temperature and surface current climatologies for the tropical Indian Ocean, while *Molinari et al.* [1990] used three different satellite-tracked drifting buoy data sets for generating mean monthly climatology of surface currents in the tropical Indian Ocean. They also computed phase and amplitude of the first two harmonics of the annual cycle of the surface currents.

Satellite altimeters are very useful for studying the ocean circulation as they provide truly global observations of sea level. Altimeter observations of sea level variations can be used for validating model results and also for improving the models. *Perigaud and Delecluse* [1992, 1993] analyzed Geosat satellite altimeter data for comparison with numerical simulations from a reduced gravity model forced by observed winds. After decomposition into complex empirical orthogonal functions, they found that the low frequency anomalies are decscribed by the first two modes for observations as well as simulations. It was also found that basin averaged observed and simulated sea level changes are well correlated over 1985-1988. However,

the accuracy of Geosat data is questionable because of the absence of onboard radiometer and also because of the poor orbit accuracy.

In the present study we have used data from Topex/Poseidon (TP) satellite for detecting large-scale low-frequency sea-level variations over the AS north of 10°S. The observed sea level variations are compared with simulations derived from a reduced-gravity model forced by observed winds. In section 2, we provide a brief description of the TP data. In section 3 we describe the model and reference runs. In section 4 we describe the complex CEOF technique and in section 5, we describe the results. The final Section discusses our conclusions.

2. ALTIMETER DATA

The data used in the study are the sea level anomaly heights observed by the TP altimeter. They were procured via anonymous FTP from the University of Texas at Austin Center for Space Research (UT/CSR) sea level data base. This data base contains $1° \times 1°$ gridded sea level anomaly heights observed by the TP every 10 days. Detailed information about data processing and error analysis can be obtained in *Tapley et al.* [1994]. We summarise the salient features.

The usual media and instrument corrections (ionosphere, wet and dry troposphere, and electromagnetic bias) and geophysical corrections (tides and inverted barometer) have been applied to the measurement. Subsequently, the altimeter measurements have been reduced to sea surface topography heights using a precise orbit computed at UT/CSR using the available Satellite Laser Ranging and DORIS Doppler tracking data. Data are interpolated to a common grid center along a high resolution mean sea surface computed from four years of TP data, then averaged into 1 ° by 1 ° grids and smoothed over 600 km wavelengths with a Gaussian weighted filter with a roll-off of three degrees. The estimated accuracy of the sea level anomalies in this data is 3 to 4 cm over the entire ocean.

The sea level anomaly (SLA) is the deviation of the sea surface away from the computed mean surface. We extract the data for two years (1993-94) consisting of 72 cycles in our region of interest which is from 10°S to 23°N and from 40°E to 75°E. The starting cycle corresponds to January 10, 1993.

3. MODEL

The ocean model used in the study is a fully nonlinear one and a half layer reduced gravity system formulated in spherical coordinates. The model is similar to the one described in *Luther and O'Brien* [1985]. The equations are

$$\frac{\partial U}{\partial t} + \frac{1}{a\cos\theta}\frac{\partial}{\partial\phi}\left(\frac{U^2}{H}\right) + \frac{1}{a}\frac{\partial}{\partial\theta}\left(\frac{UV}{H}\right) - (2\Omega\sin\theta)V = -\frac{g'}{2a\cos\theta}\frac{\partial H^2}{\partial\phi} + \frac{\tau^\phi}{\rho_1} + A\nabla^2 U - \gamma U \tag{1}$$

$$\frac{\partial V}{\partial t} + \frac{1}{a\cos\theta}\frac{\partial}{\partial\phi}\left(\frac{UV}{H}\right) + \frac{1}{a}\frac{\partial}{\partial\theta}\left(\frac{V^2}{H}\right) + (2\Omega\sin\theta)U = -\frac{g'}{2a}\frac{\partial H^2}{\partial\theta} + \frac{\tau^\theta}{\rho_1} + A\nabla^2 V - \gamma V \tag{2}$$

and

$$\frac{\partial H}{\partial t} + \frac{1}{a\cos\theta}\left[\frac{\partial U}{\partial\phi} + \frac{\partial}{\partial\theta}(V\cos\theta)\right] = -\gamma(H - H_0). \tag{3}$$

Here $U = uH$ and $V = vH$ represent the eastward and northward components of the upper-layer transport, respectively, where, u and v are the depth-independent eastward and northward velocity components in the upper layer, and H the upper layer thickness. Further, a is the radius of the earth, Ω is its angular velocity, g' is the reduced gravity. Its value is .03 m s^{-2}. A is the horizontal eddy viscosity and its value is 10000 m ^{2} s^{-1}.The wind forcing $\tau = (\tau^\phi, \tau^\theta)$ is a body force acting over the upper layer and ρ_1 (=1023 kg m^{-3}) is the density of the layer. γ represents a damper to be explained later and H_0 is the initial upper layer

thickness (=200 m). The ocean basin extends from 29°S to 23°N in latitude and from 40°E to 75°E east in longitude. The horizontal resolution is 0.5° on an Arakawa C-grid in both latitudinal as well as longitudinal directions. The equations are integrated in time using a leapfrog scheme with a time step of 15 minutes. Every 19 time steps values of variables at two successive time levels are averaged in order to suppress the time-splitting instability. Realistic coastline geometry is used. All the boundaries are closed with no-slip conditions. However, from 29°S to 10°S, the wind stress has been damped using a cosine damper and the horizontal friction has been increased as in *Perigaud and Delecluse* [1992]. Thus this band is a sponge layer and our analysis will be restricted to the region northwards of 10°S.

Part of the eastern boundary of the model region is open ocean. Since we have applied no-slip boundary condition at the entire eastern boundary, we include a damper near the eastern boundary that efficiently absorbs incoming radiation [*McCreary and Kundu*, 1989]. All the fields are damped near the eastern boundary. The damping coefficient γ,which is same for all the variables U, V and H, is zero except within 2.5° of the open part of the eastern boundary, where it increases linearly to a distance of 1.5° and is constant thereafter. The maximum strength of damping used is 1 day^{-1}.

The wind data used for forcing the model are derived from the monthly pseudo wind-stress data from the Florida State University, Tallahassee. These data cover the entire Indian Ocean with a resolution of 1° [*Legler et al.*, 1988]. These data have been converted into wind stress utilizing a constant drag coefficient of 1.3 $\times 10^{-3}$. The model is spun up from rest for 6 years using the 1977-1992 mean of monthly wind fluctuations. After this initial spin-up, the model has been run for four years starting from January 10, 1993. We have computed a four year mean interface depth for consistency with the analysis of the TP data. This is required for calculating SLA, which is the quantity observed by Topex. We store the model results for two years starting from 10th January 1993 at every 10 day intervals.

We have also used another version of the model where the damping near the eastern boundary is extended to the whole eastern boundary. This run suppresses activity along the coast of India, allowing for identification of coastally generated wind-forced waves.

CEOF TECHNIQUE

This technique is generally applied to the analysis of two-dimensional data sets for resolving the dominant propagating modes of variability [*Barnett*, 1983; *Shriver et al.*, 1991]. Propagating structures are extracted from a data set by decomposing the data into complex empirical orthogonal functions and by sorting out the dominant modes in order of decreasing variance. This technique has been applied to the detection of low-frequency propagating Rossby wave signals off the eastern Pacific coast [*Shriver et al.*, 1991] and for analyzing sea level variations in the tropical Indian Ocean from Geosat altimeter and shallow water simulations [*Perigaud and Delecluse*, 1992, 1993].

Let us denote a time-varying data field by $d(x, y, t)$ where (x, y) denotes spatial position and t is time. We denote by $D(x, y, t)$ a complex data field, the real part of which is the original data field and the imaginary part is the quadrature (Hilbert transform) of the data. The latter is nothing but the data field, phase advanced by 90 ° in time. More specifically, if the data field $d(x, y, t)$ has the Fourier representation of the form

$$d(x, y, t) = \sum_{\omega} a(x, y, \omega) cos\omega t + b(x, y, \omega) sin\omega t \tag{4}$$

then the Hilbert transform $d_h(x, y, t)$ can be represented as

$$d_h(x, y, t) = \sum_{\omega} b(x, y, \omega) cos\omega t - a(x, y, \omega) sin\omega t \tag{5}$$

Then $D(x, y, t)$ can be written as

$$D(x,y,t) = d(x,y,t) + id_h(x,y,t) \tag{6}$$

The next step in the analysis is the formation of the covariance matrix of the data field $D(x,y,t)$. Let C denote the covariance matrix which is Hermitian and positive-definite by construction. It thus possesses real positive eigenvalues and a set of orthogonal complex eigenvectors $b_n(x,y)$. Hence $D(x,y,t)$ can be represented as

$$D(x,y,t) = \sum_n a_n(t) b_n^*(x,y) \tag{7}$$

where the asterisk implies complex conjugation. The functions $b_n(x,y)$ will be referred to as spatial functions. The principal components $a_n(t)$ are obtained as

$$a_n(t) = \sum_{x,y} D(x,y,t) b_n(x,y) \tag{8}$$

and will be referred to as temporal functions. In actual practice these will be finite- dimensional vectors because of the discrete representation of the data set.

From each eigenmode n, four measures can be defined for representing possible moving features in the data. The spatial amplitude function $S_n(x,y)$ represents the spatial distribution of variability associated with each eigenmode, and the spatial phase function $\theta_n(x,y)$ shows the relative phase of fluctuation among the various spatial locations where the data field d is defined. Similarly, the temporal amplitude function $R_n(t)$ and the temporal phase function $\phi_n(t)$ provide measures of temporal variability associated with each eigenmode. The time-derivative of $\phi_n(t)$ is a measure of frequency, and the spatial gradient of the spatial phase function $\theta_n(x,y)$ provides the local wavenumbers in x and y directions.

In the present study, we have applied the CEOF technique to the analysis of TP and

model SLA in the region bounded zonally between 23°N and 10°S and meridionally between 40°E and 75°E and from January 10, 1993 to December 15, 1994.

RESULTS

Full Model

It is well known that reduced gravity models can simulate the semiannual reversal of the Somali current and the gyre circulations in the AS fairly well [*Luther and O'Brien*, 1985; *McCreary et al.*, 1993]. The model developed by us in this study has also produced an annual cycle with these circulation features.

The model SLA on July 17, 1993 (Fig. 1) contains an eddy structure represented by contours of large positive anomaly in the region between the equator and about 10°N and from 48°E to 55°E. South of the equator positive anomalies are seen in almost the entire basin except in a very narrow zonal strip between 40°E to 55°E. Coastal upwelling represented by negative anomalies is present along the Somali coast due to the prevailing southwesterly wind. On July 19, 1994, many of the structures are the same as the previous year with only minor differences. The eddy structure, however, is stronger and a strong positive anomaly is present to the east. This may be due to difference in wind between the years 1993 and 1994. Negative anomalies near the western coast of India are stronger than in 1993. In the north Arabian Sea anomalies are mostly negative. An anticyclonic circulation feature seems to be present in the year 1994.

The sea level anomalies on Dec. 13, 1993 are opposite to the summer case except in the north Arabian Sea. The regions of positive and negative anomalies in the western and southern parts have been interchanged because of the reversal in the wind direction. The model result of Dec 15, 1994 is almost the same as those of Dec 13, 1993 with minor changes. Anticyclonic circulation feature is present in the north Arabian Sea in both the years.

Time-longitude plots of model SLA at 15°N, 10°N and 10°S (Fig. 2) show varying degrees of westward propagation suggesting Rossby waves. The estimated phase speeds are 10 cm s^{-1} at 15°N , 17 cm s^{-1} at 10°N and 29 cm s^{-1} at 10°S. At 15°N and 10 °N, alternating bands of positive and negative SLA are present near the Somali coast, representing upwelling and downwelling because of the two opposite monsoon regimes. To the east, the sea level anomalies are of opposite sign. More specifically, at 15°N and at 10°N we see that from January 10, 1993 till the end of April, 1993 there is positive sea level anomaly near the Somali coast and with the advent of southwest monsoon, i.e. from the beginning of May 1993 till the end of September 1993, the anomalies near the coast turn negative. Upwelling wave propagation is evidenced at 15°N from the western coast of India to 60 °E. In the year 1993 it begins at the western coast of India in the end of June. Propagation of downwelling waves is evidenced between the same longitudes and begins at the western coast of India in the end of January, 1994. Upwelling wave propgation again starts at the western coast of India in the end of June 1994. Positive SLA persists in the region 52 °E to 70 °E from the middle of May till the middle of October in both the years. At 10 °S we see seasonally varying patterns of wave propagation across the whole basin. Upwelling wave generation at the eastern boundary of the basin spans the period from the beginning of January till the end of April in both the years. Generation of downwelling waves at the eastern boundary is seen at other times of the year.

Damped Model

To better understand the generation of the Rossby waves along the west coast of India, we have used a version of the model where the damping has been extended along the entire eastern boundary. A time-longitude plot of the difference in SLA simulated by the two versions at 15°N is shown in Fig. 3. This difference plot shows westward wave propagation, with an estimated speed about 10 cm s^{-1}. The difference in SLA is of the order of 1 to 2 cm. The wave generation at the western coast of India spans the period from June to September in 1993

and from April to July in 1994. Differences also occur at the western boundary of the model with strong negative values peaking at the end of August of both the years. At 10°N, there are very weak differences between the two versions of the model. There is no significant difference between the two models below 10°N.

Altimetry

The altimetric map on July 17, 1993 (Fig. 4) shows large positive anomalies near the Arabian coast between the equator and 6°N. This is the signature of the Great Whirl, which occurs during monsoon months. The contours are, however, not closed and the negative anomalies near the coast are not picked up by the TP data set we analyze. There are negative anomalies near the western coast of India and positive anomalies in the southeastern and northwestern parts of the domain. The map on July 19, 1994 shows similar features with the important difference that the large positive anomaly in the northwestern part is absent. The model does not show this positive anomaly in either year.

The SLA on Dec 13, 1993 is dominated by negative anomalies. The change in the anomaly gradient indicates reversal of the currents, largely due to the changing wind pattern. On Dec 15, 1994 the positive anomalies near the western coast of India have disappeared, but a strong band of positive anomaly has appeared at the southeastern part of the basin.

A time-longitude plot at 15°N shows that the SLA changes sign from positive to negative with the change of season. From the end of January till the end of May, the SLA is positive in both the years, while it is negative during the other months. A similar trend is observed at 10°N (Fig. 5). However, there is evidence of wave propgation in the eastern half of the basin and the estimated speed of propagation is 16.8 cm s^{-1}. At 10°S we observe wave propagation from the end of April 1994 till the beginning of September of the same year across the whole basin. The estimated speed of propagation is about 25 cm s^{-1}.

CEOF1 – The annual cycle

The first CEOF contains 71% of the variance for the model and 58% for Topex. The temporal phases for both model and TP (Fig. 6) indicate an annual frequency. Since the origin of phase can be chosen arbitrarily, we have adjusted the initial temporal phase of the model to match the TP result. Correlation between observed and simulated phases is 0.82. Agreement between simulated and observed temporal magnitudes is, however, not high although an annual signal is present in both the model as well as TP results. The spatial amplitudes for the model as well as TP (Fig. 7) show large signals in the western part of the AS. Patterns of strong amplitude are present in the region between 2°N and 8°N and from 50°E to about 57°E for both the model as well as TP. TP does not contain the coastal current. Both the model as well as TP spatial amplitudes show anticyclonic circulation features in the Northern AS, though it is less clear for TP. The model spatial phase (Fig. 7) indicates poleward propagation of phase outside the equatorial waveguide. However, in the TP phase the propagation is polewards in the southern part. Westward propagation of phase is also evidenced in certain parts of the region in both simulated as well as observed spatial phases. Specifically, this propagation is seen in the eastern equatorial waveguide and in the north AS.

The large-scale circulation in the model AS reverses with the seasons due to the Indian Monsoon. The summer typically has two strong regions of anticyclonic circulation, the first is just east of Somalia, the second in the northern AS Fig. 8. The opposite circulation pattern prevails in winter. A similar reversal is seen between 10°S and the equator. The same reversal is seen in the TP altimetry (figrefceof1topex). Again, a strong anticylonic circulation exists east of Somalia, but the circulation in the northern AS is weak and does not exhibit even a hint of closed streamlines.

In Fig. 10 and Fig. 11 we present the results along 15°N, 10°N and 10°S for observation as well as simulation. At 15°N, both the model and TOPEX show alternating band of positive

and negative SLA at the western part of the basin. In the eastern part there is evidence of westward wave propagation in both simulation as well as observation. At 10°S, there is a striking similarity between model and observation with evidence of westward phase propagation across the basin. At 15°N , the estimated phase speed is 10 cm s^{-1} from simulation and 9.33 cm s^{-1} from observation. At 10 °S, the estimated phase speed is 21 cm s^{-1} from simulation while the same speed is estimated from observation.

CEOF2 – The semiannual cycle

In Fig. 12 we present the amplitude of the temporal functions for the second CEOF for the model and observations. There is good agreement between these two with a correlation of 0.47. A semi-annual frequency is indicated. The agreement between phase plots is also quite good and again a semiannual frequency is seen to be present. The amplitude plots show similarity in structure in the region between equator and 10°N. However, the recirculating structures present in the simulations are absent in the observations. The phase plots show dominant westward and poleward propagation of phase in the latitude band from equator to 10°N in both simulations as well as observations. In the southwestern part of the basin there is poleward propagation of phase in both the cases and in the southeastern part there is westward and equatorward propagation in both the cases.

Summary and Discussion

A reduced gravity model of the Arabian Sea is driven with the FSU winds, model sealevel is calculated and compared to altimetry data from TP. Both show a strong seasonal cycle. The model is of limited domain, isolating the AS from influences from the eastern Indian Ocean. Model results south of 10°S are not examined due to distortions from the boundaries of the limited domain and damping of the winds below this latitude.

The largest variations in the model are in the western Indian Ocean along the coast of Somalia, where the Somali Current reverses seasonally with the monsoon. This current and its reversal extends along the coast of Saudi Arabia, generating cyclonic vorticity in the northern AS during winter, and a cyclonic-anticyclonic pair in summer (Fig. 1).

Rossby waves are a major source of variation in the model away from the western boundary (Fig. 2). Some of these are generated within the basin of the AS and some are generated along the western coast of India. The difference fields between the undamped and damped model (Fig. 14) indicate the coast of India north of roughly 12°N is a source of a downwelling Rossby waves generated in the summer. The generation of this seasonal Rossby wave is coincident with the generation of a coastally trapped Kelvin wave which travels cyclonically around the AS (Fig. 14). This wave is responsible for the variations in the western basin in Fig. 3 which are approximately 25% of the amplitude of the full seasonal cycle.

The southwest coast of India does not produce wind-generated Rossby waves in the model. Along 10°N there is little sign of propagating wave activity. This is confirmed in the CEOF analysis.

The first CEOF mode, CEOF1, of the model is dominated by the seasonal cycle and comprises 71% of the total variance. The corresponding spatial function is predominantly composed of the Somali Current, Great Whirl and circulation in the northern AS. Westward propagation can be seen in the phase of the spatial function (Fig. 7) in the northern AS as a series of nearly meridional phase lines. This is confined to a region north of about 12°N. There is also indication of westward propagation along, and just south of, the eastern equator. South of the equator the phase lines are sloped, indicating both zonal and northward propagation.

The annual cycle in the TP data, as represented by its CEOF1, has only general similarities to that from the model. The lack of a coastal current in the TP data greatly effects

the structure of the spatial function (Fig. 7), which is dominated by a region of high loading projecting eastward from the coast of Somalia. The peak anticyclonic signature within this tongue is very similar to that in the model CEOF1, except the TP spatial function does not contain closed isolines in this area. Neither the model nor the TP result contain a strong phase gradient in this region (although the model spatial phase function does have a weak north-south gradient) suggesting a stationary feature. This is consistent with the identification of this feature with the Great Whirl.

The tongue in the TP CEOF1 projects towards southwest India where is achieves a secondary maximum around 7°N. This secondary maximum may be related to a Rossby wave signal coming in from the Bay of Bengal, probably wrapping around the tip of India as a coastally trapped Kelvin wave. The spatial function of the model, which cannot reproduce such a signal, does not possess this secondary maximum. The propagating nature of this feature in the TP data is suggested from the horizontal gradient of the spatial phase function in Fig. 7.

The semi-annual signal is captured by CEOF2. There is better agreement between the model and TP results for this mode than for CEOF1. Both CEOF2 spatial magnitudes contain a region of high variance extending eastward from Africa, though in the model this region is a few degrees north of its location in the TP analysis.

In summary, the Arabian Sea has a strong seasonal cycle, not all of which is detectable in the TP dataset analyzed here. This seasonal cycle is composed of propagating and non-propagating features. The former are generated within the basin as well as along the northwest coast of India. A strong signal, possibly from the Bay of Bengal, appears in the TP data, but not in the model results. Inclusion of the Bay of Bengal in future models appears to be essential for an accurate representation of the circulation in the Arabian Sea.

Acknowledgments. This work was supported by the Office of Naval Research, Secretary of

the Navy Grant Number N00014-1-0369 which provides the base support for the research conducted by Professor James J. O'Brien, Director, The Center for Ocean-Atmospheric Prediction Studies, at The Florida State University. In addition support was received from NASA Headquarters, NASA Grant Number NA46GP0114.

References

Barnett, T. P., Interaction of the monsoon and Pacific trade wind system at interannual time scales, 1, the equatorial zone, *Mon. Wea. Rev.*, *111*, 756–773, 1983.

Kindle, J. C., and J. D. Thompson, The 26- and 50-day oscillations in the western Indian Ocean: Model results, *J. Geophy. Res.*, 4721–4736, 1989.

Legler, D. M., I. M. Navon, and J. J. O'Brien, Objective analysis of pseudo-stress over the Indian ocean using a direct-minimization approach, *Mon. Wea. Rev.*, *117*, 709–720, 1988.

Luther, M. E., and J. J. O'Brien, A model of the seasonal circulation in the Arabian Sea forced by observed winds, *Prog. Oceanog.*, *14*, 353–385, 1985.

McCreary, J. P., and P. K. Kundu, A numerical investigation of the Somali current during the Southwest monsoon, *J. Mar. Res*, 25–28, 1988.

McCreary, J. P., and P. K. Kundu, A numerical investigation of sea surface temperature variability in the Arabian Sea, *J. Geophy. Res.*, *94*, 16,097–16,114, 1989.

McCreary, J. P., P. K. Kundu, and R. L. Molinari, A numerical investigation of dynamics, thermodynamics and mixed-layer processes in the Indian Ocean, *Prog. Oceanog.*, *31*, 181–244, 1993.

Molinari, R. L., D. Olson, and G. Reverdin, Surface current distributions in the tropical Indian Ocean derived from compilations of surface buoy trajectories: The Indian Ocean drifters, *J. Geophy. Res.*, *95*, 7217–7238, 1990.

Perigaud, C., and P. Delecluse, Annual sea level variations in the Southern Tropical Indian Ocean from Geosat and shallow-water simulations, *J. Geophy. Res.*, *97*, 20,169–20,178, 1992.

Perigaud, C., and P. Delecluse, Interannual sea level variations in the Tropical Indian Ocean from Geosat and shallow water simulations, *J. Phys. Oceanogr.*, *23*, 1916–1934, 1993.

Rao, R. R., R. L. Molinari, and J. F. Festa, Evolution of climatological near-surface thermal structure of the tropical Indian Ocean, 1. description of mean monthly mixed layer depth, and sea surface temperature,surface current, and surface meteorological fields, *J. Geophy. Res.*, *94*, 10,801–10,815, 1989.

Schott, F., Recent studies of western Indian Ocean circulation, in *Further Progress in Equatorial Oceanography*, edited by E. J. Katz and J. Wittie, 287–302, Nova University Press, Damia, Florida, 1987.

Shriver, J. F., M. A. Johnson, and J. J. O'Brien, Analysis of remotely forced oceanic rossby waves off california, *J. Geophy. Res.*, *96*, 749–758, 1991.

Simmons, R. C., M. E. Luther, J. J. O'Brien, and D. M. Legler, Verification of a numerical ocean model of the Arabian Sea, *J. Geophy. Res.*, 15,437–15,453, 1988.

Tapley, B. D., D. P. Chambers, C. K. Shum, R. J. Eanes, and J. C. Ries, Accuracy assessment of the large-scale dynamic ocean topography from TOPEX/POSEIDON altimetry, *J. Geophy. Res.*, *99*, 24,605–24,617, 1994.

List of Figures

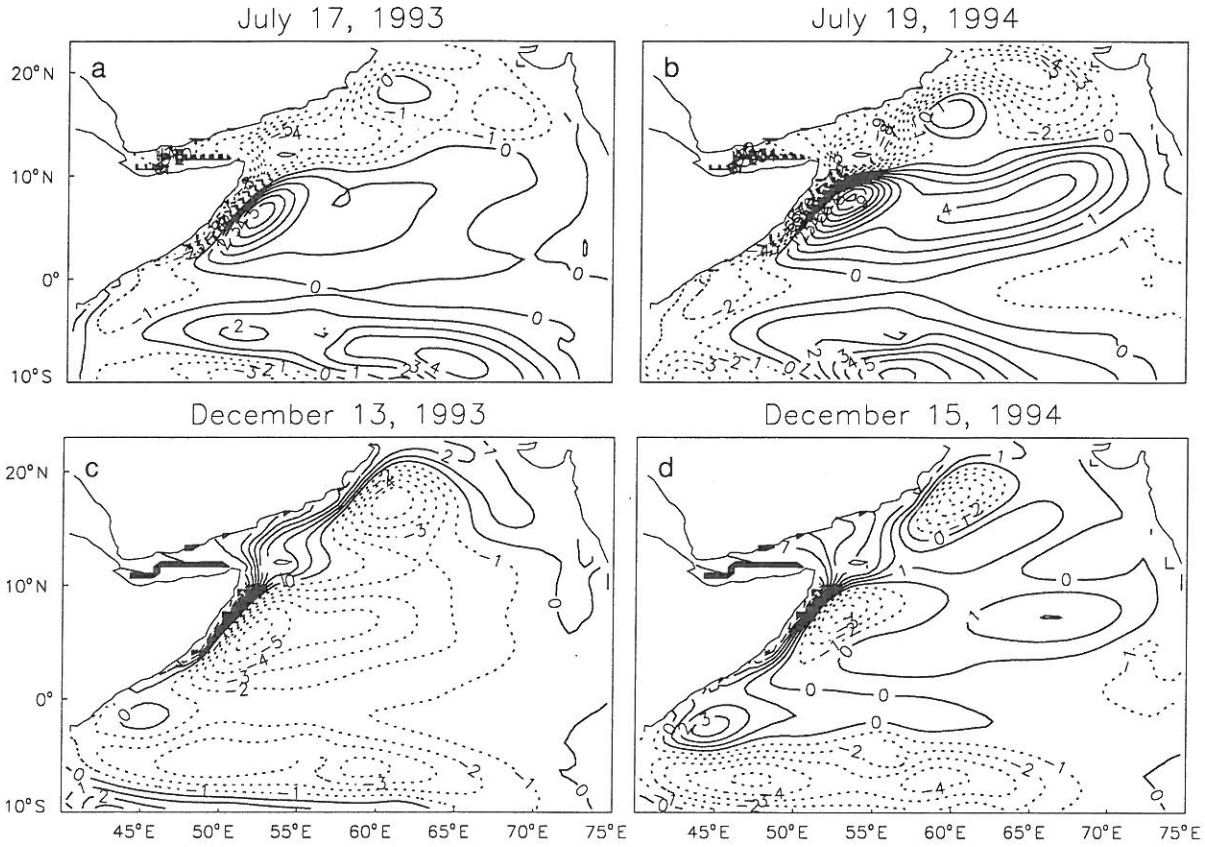

Figure 1. The sea level variations simulated by the model on (a) 17th July, 1993, (b) 19th July, 1994, (c) 13th December, 1993, and (d) 15th December, 1994.

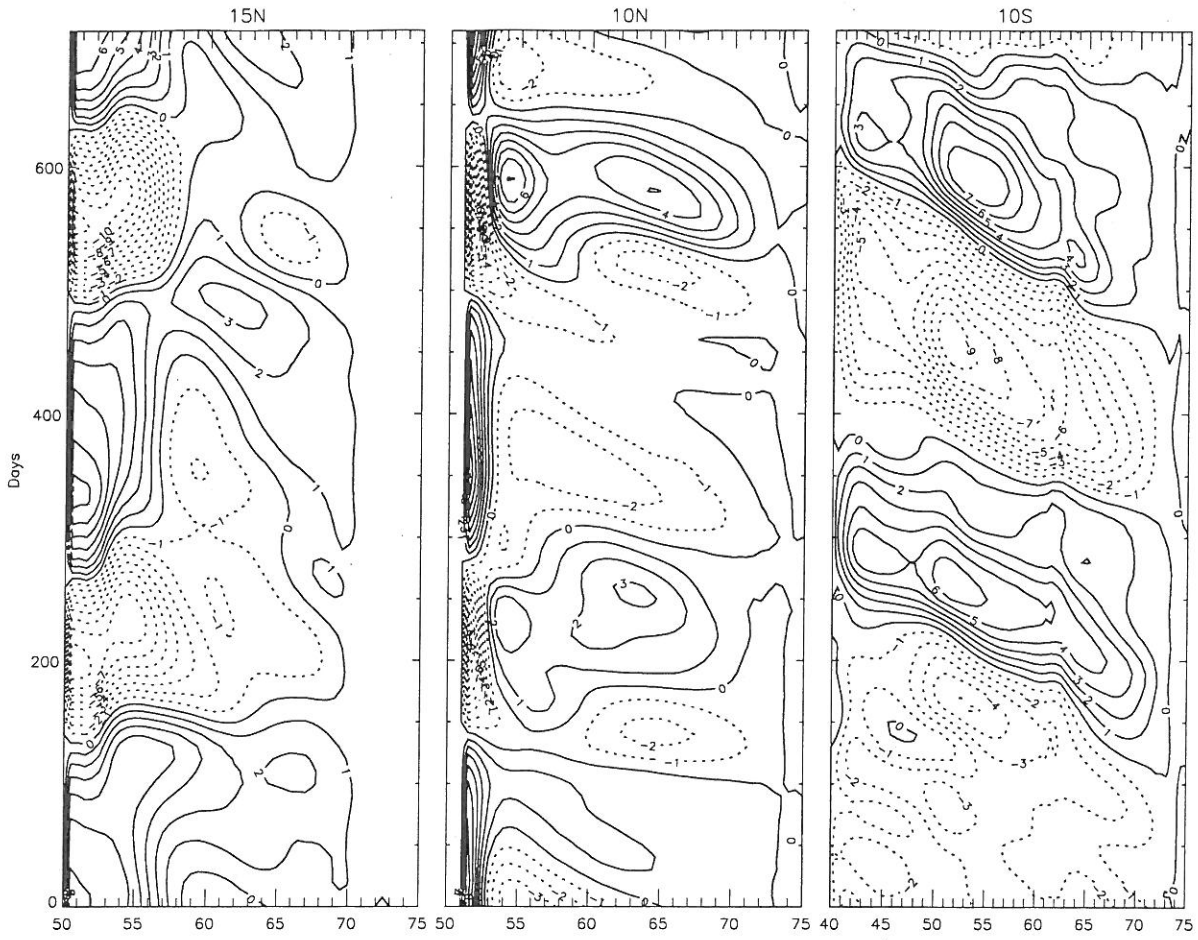

Figure 2. The model simulated sea level variations as a function of longitude and time at (a) 15°N, (b) 10°N, and (c) 10°S.

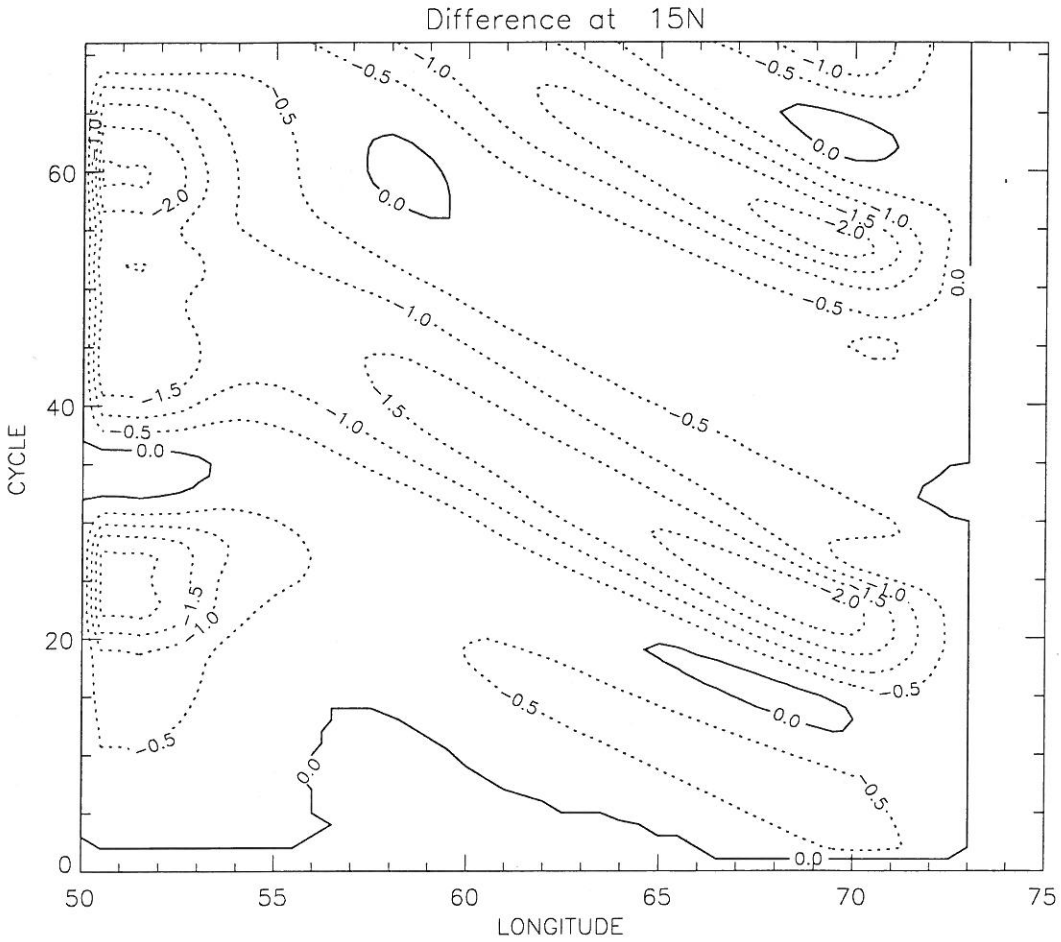

Figure 3. Time-longitude plot of the difference in sea level simulated by the full and damped versions of the model.

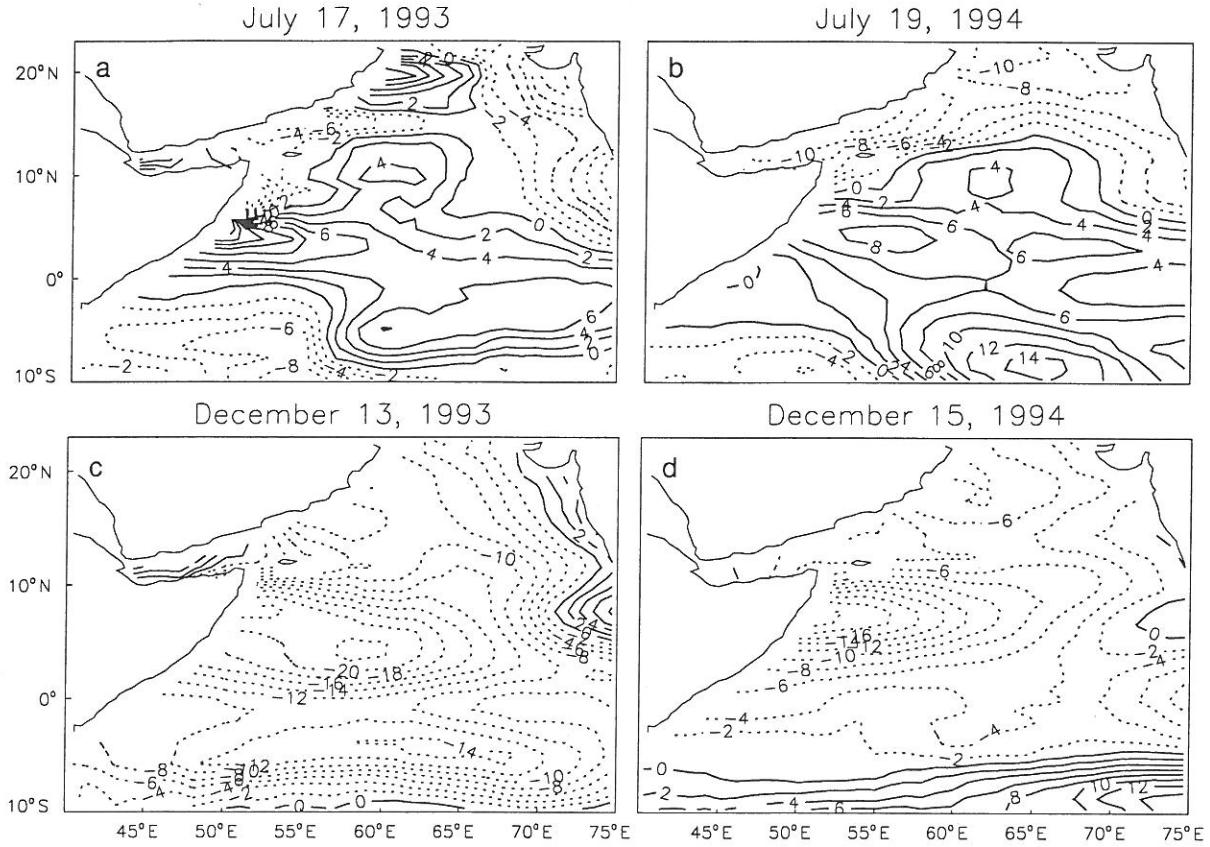

Figure 4. The sea level variations observed by TP on (a)17th July, 1993, (b) 19th July, 1994, (c) 13th December, 1993, and (d) 15th December, 1994.

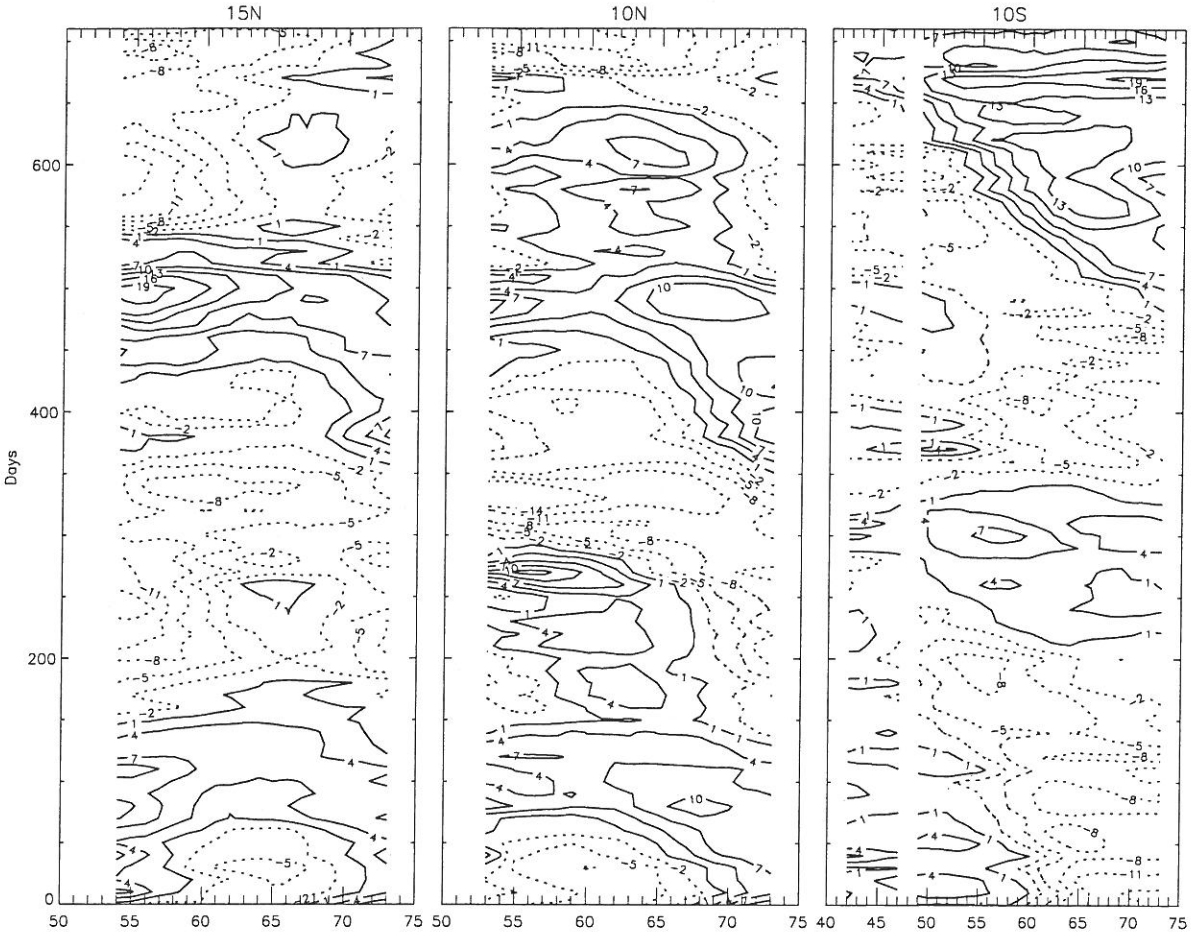

Figure 5. Sea level variations observed by TP as a function of longitude and time at (a) 15°N, (b) 10°N, and (c) 10°S.

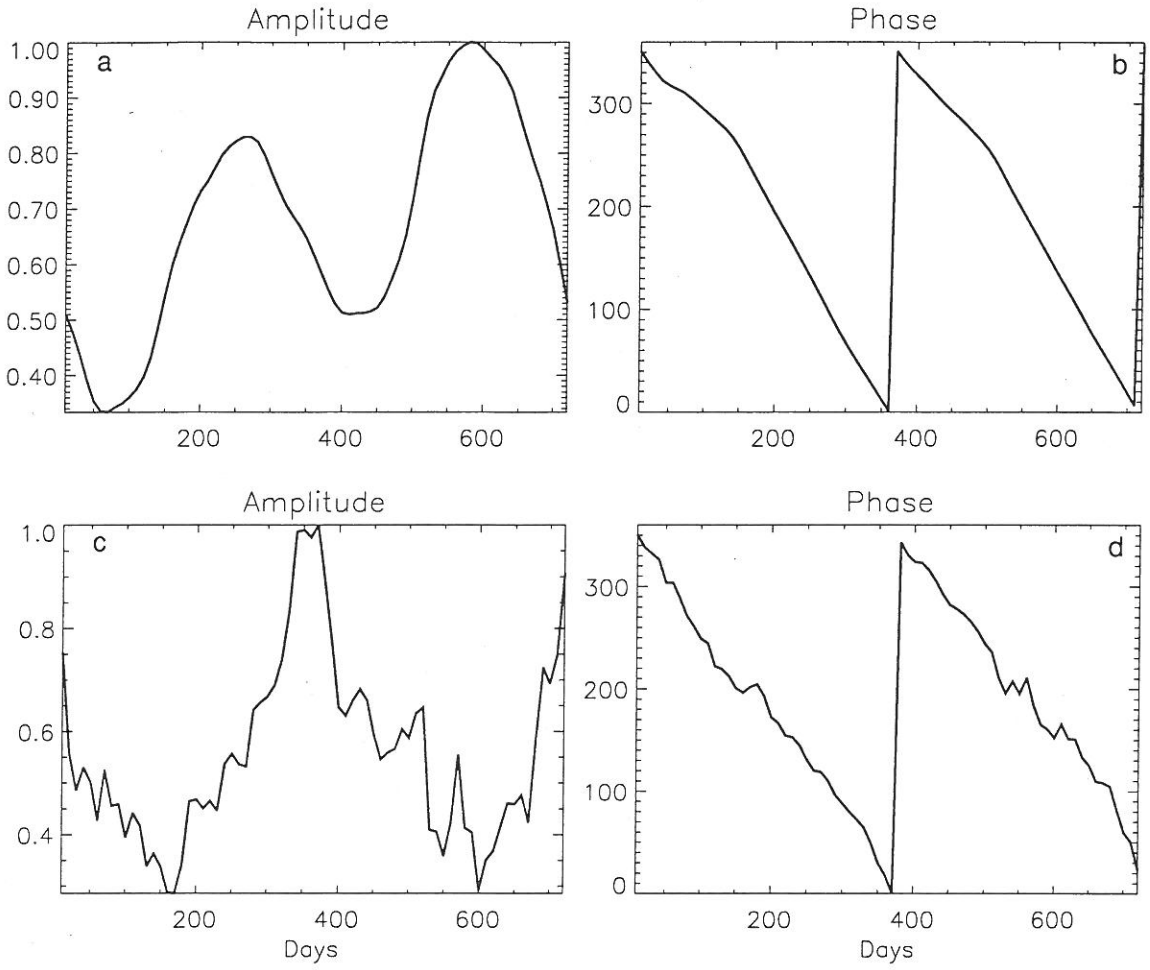

Figure 6. Temporal function of the first CEOF principal component for the model simulated and TP observed sea level anomaly. Day 0 corresponds to 10th January, 1993. (a) Model Amplitude, (b) Model Phase, (c) TP Amplitude, and (d) TP Phase. Amplitudes are normalized and phases are in degrees.

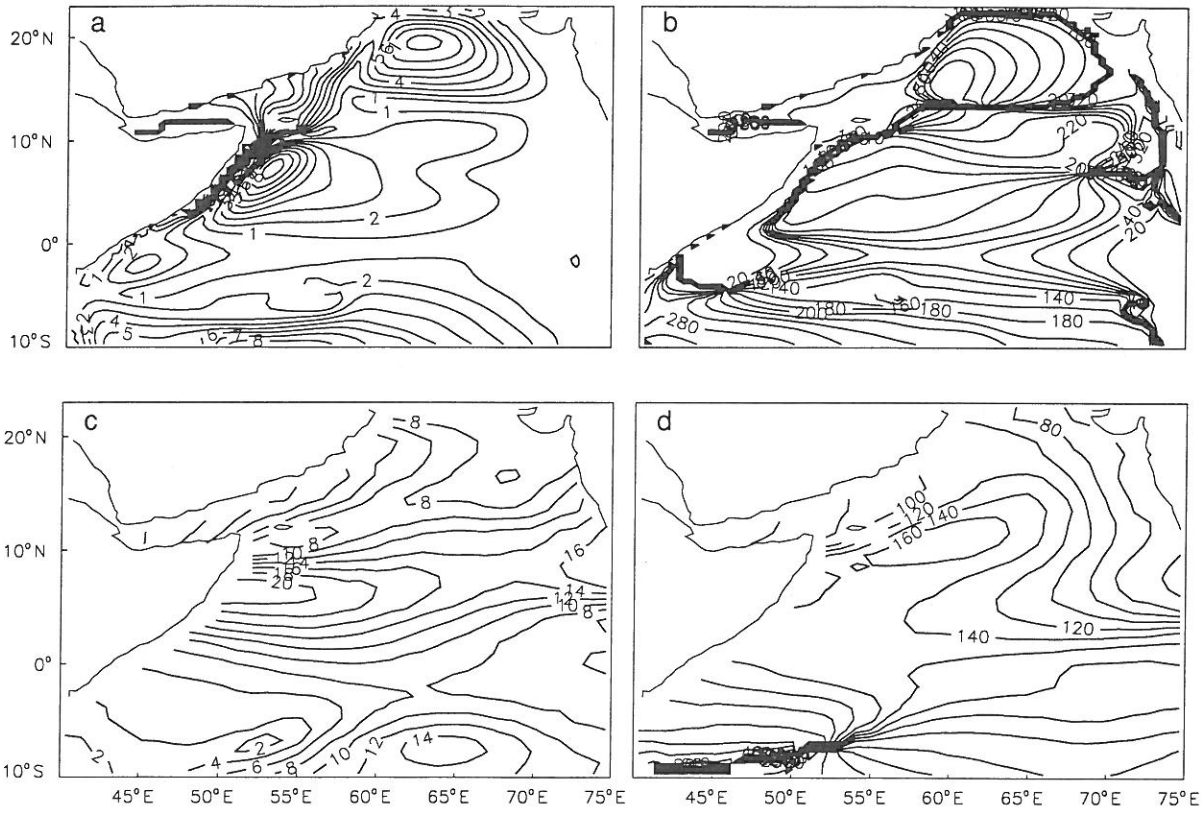

Figure 7. Spatial patterns of the first CEOF eigenvector for the sea level anomaly. (a) Model Amplitude, (b) Model Phase, (c) TP Amplitude, and (d) TP Phase.

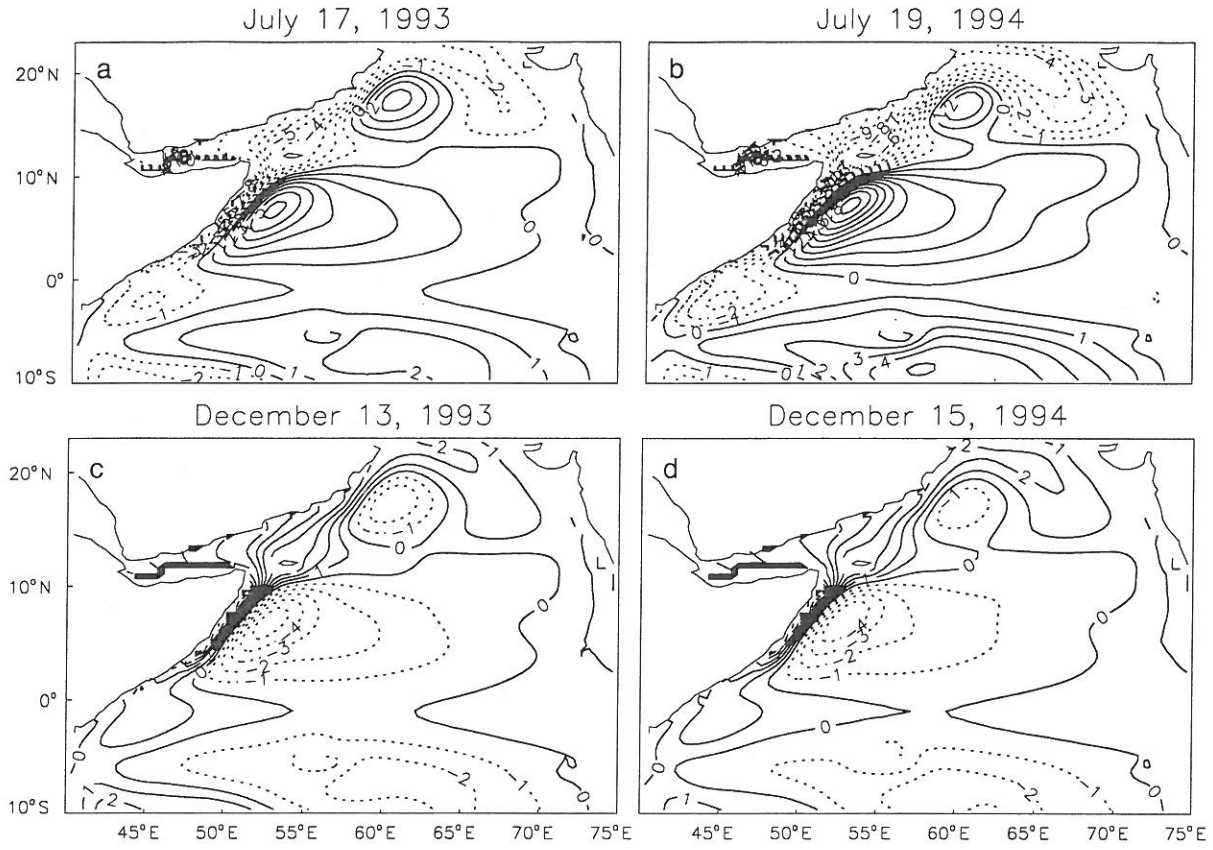

Figure 8. The model sea level variations contained in the first CEOF on (a) 17th July, 1993, (b) 19th July, 1994, (c) 13th December, 1993, and (d) 15th December, 1994.

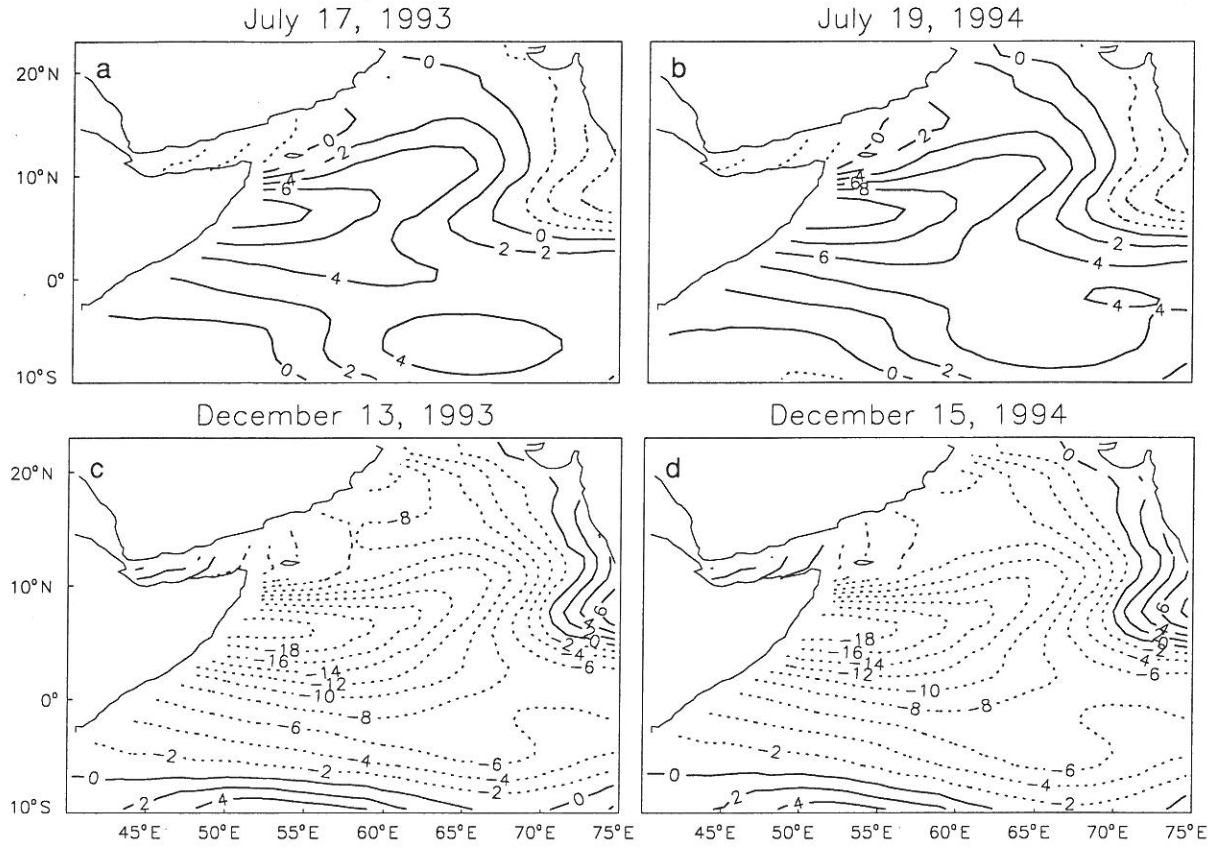

Figure 9. The TP observed sea level variations contained in the first CEOF on (a) 17th July, 1993, (b) 19th July, 1994, (c) 13th December, 1993, and (d) 15th December, 1994.

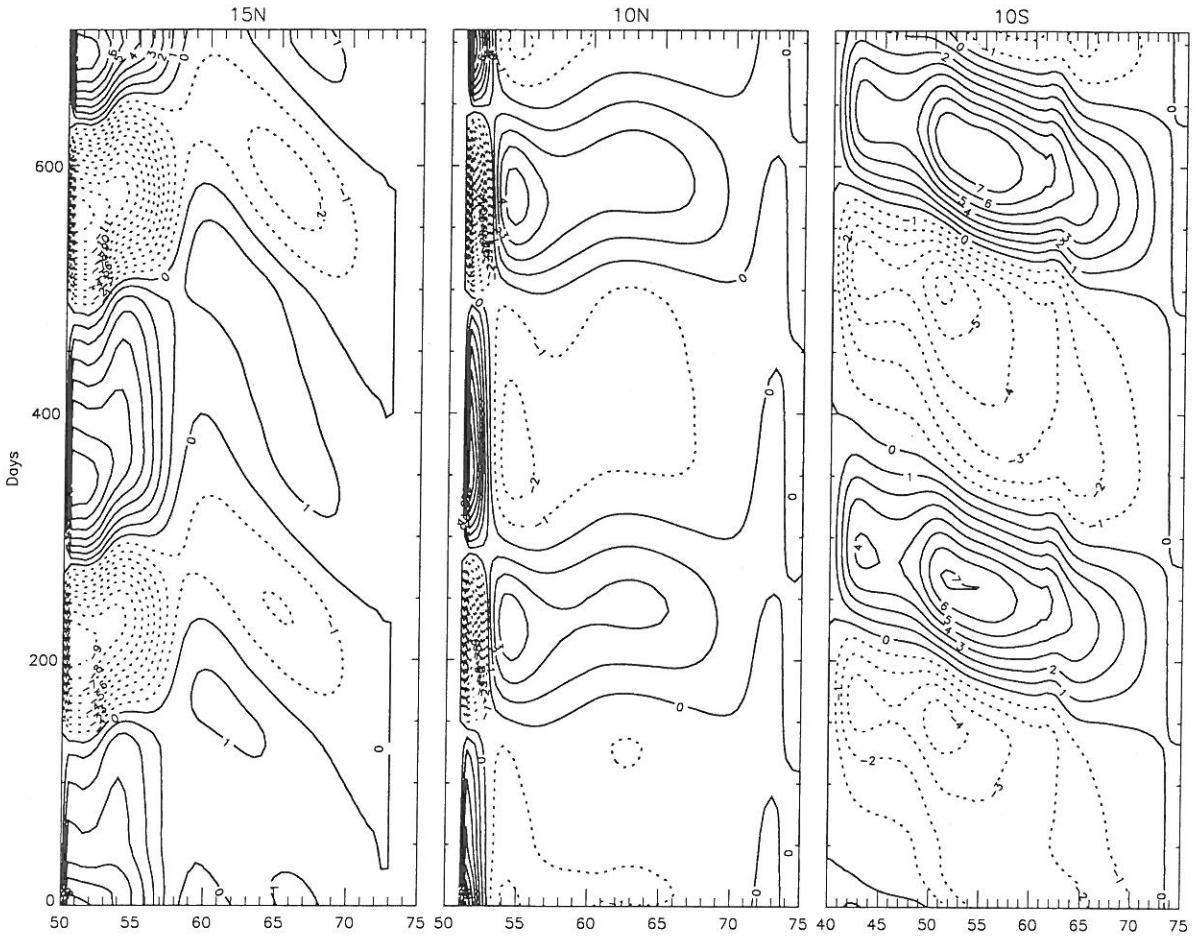

Figure 10. The model sea level variations contained in the first CEOF as a function of longitude and time at (a) 15°N, (b) 10°N, and (c) 10°S.

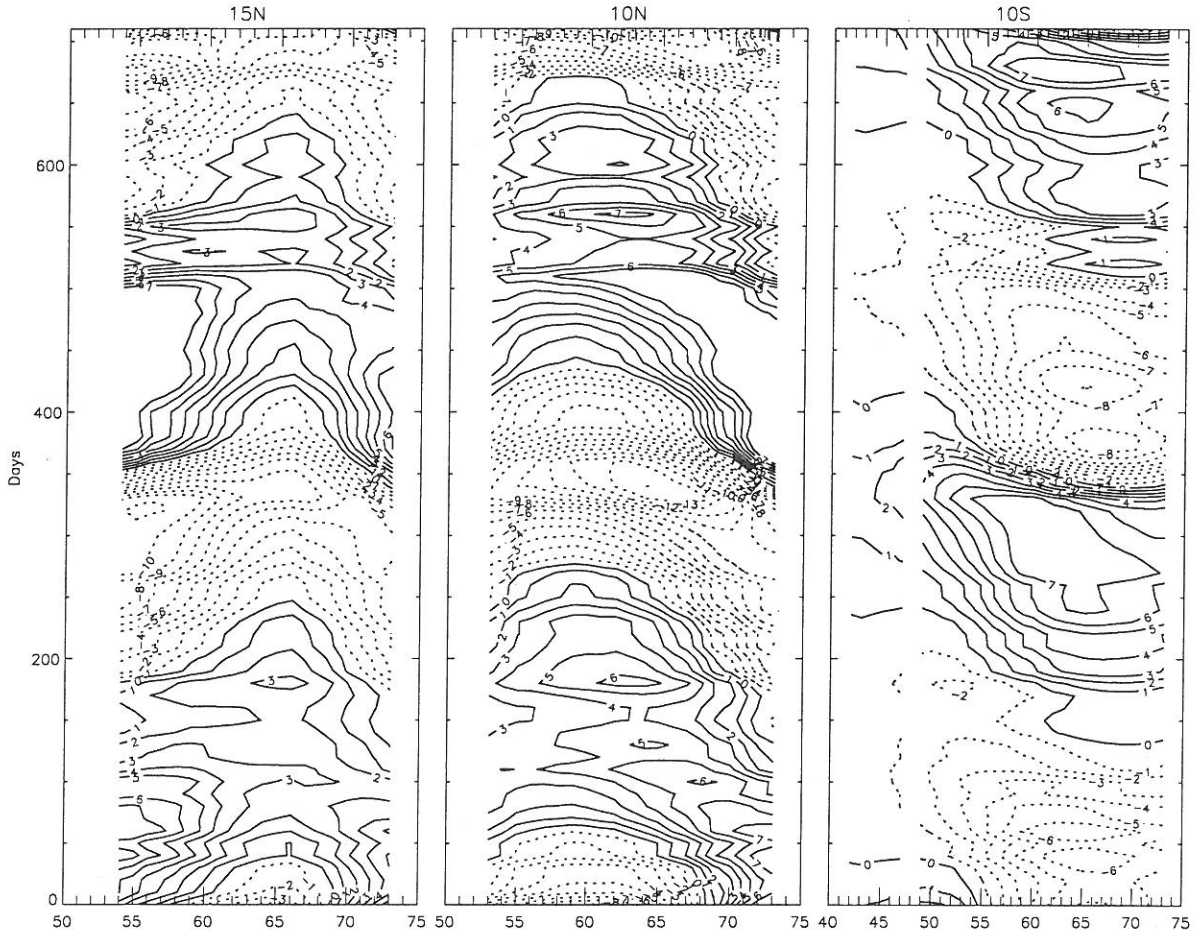

Figure 11. The TP sea level variations contained in the first CEOF as a function of longitude and time at (a) 5°N, (b) 10°N, and (c) 10°S.

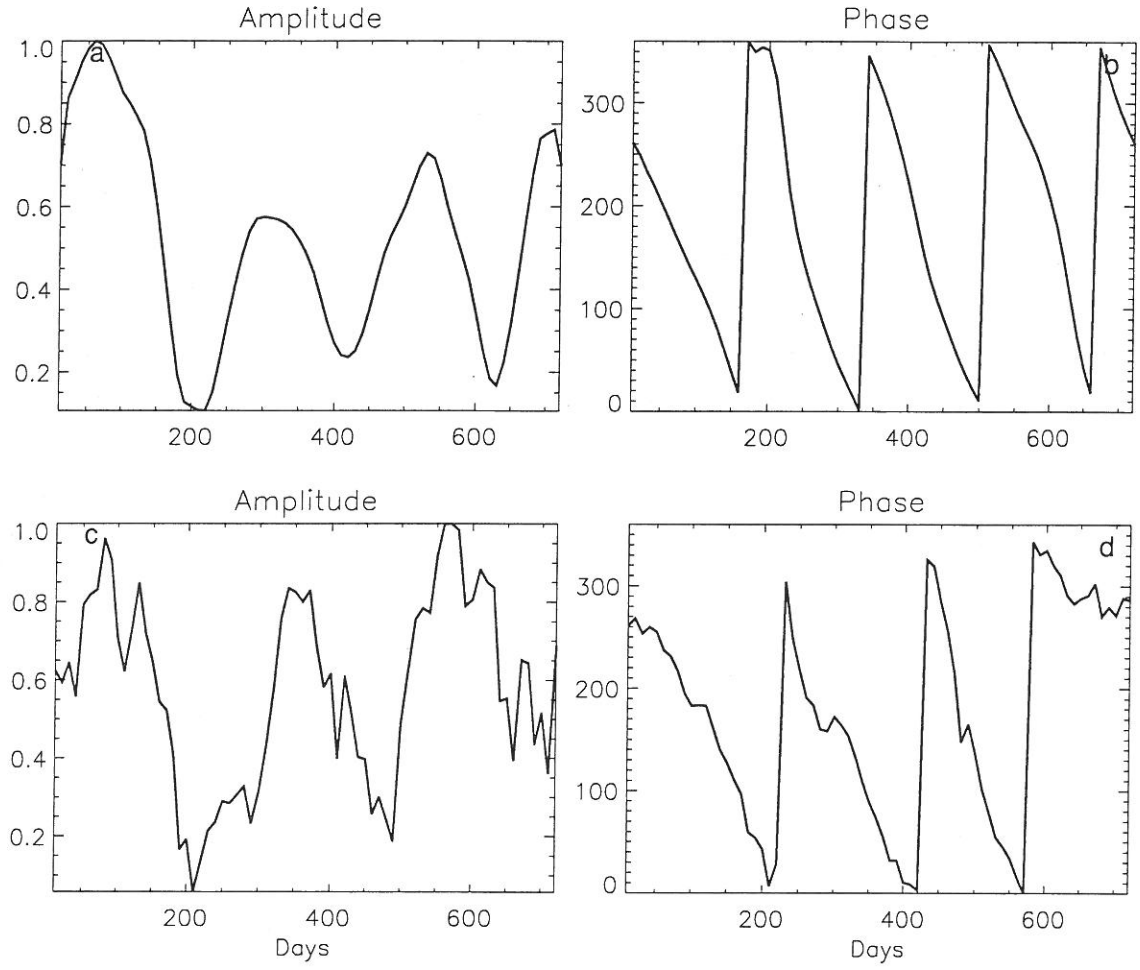

Figure 12. Temporal function of the second CEOF for the model and TP observed sea level anomaly. Day 0 corresponds to 10th January, 1993. (a) Model Amplitude, (b) Model Phase, (c) TP Amplitude, and (d) TP Phase. Amplitudes are normalized and phases are in degrees.

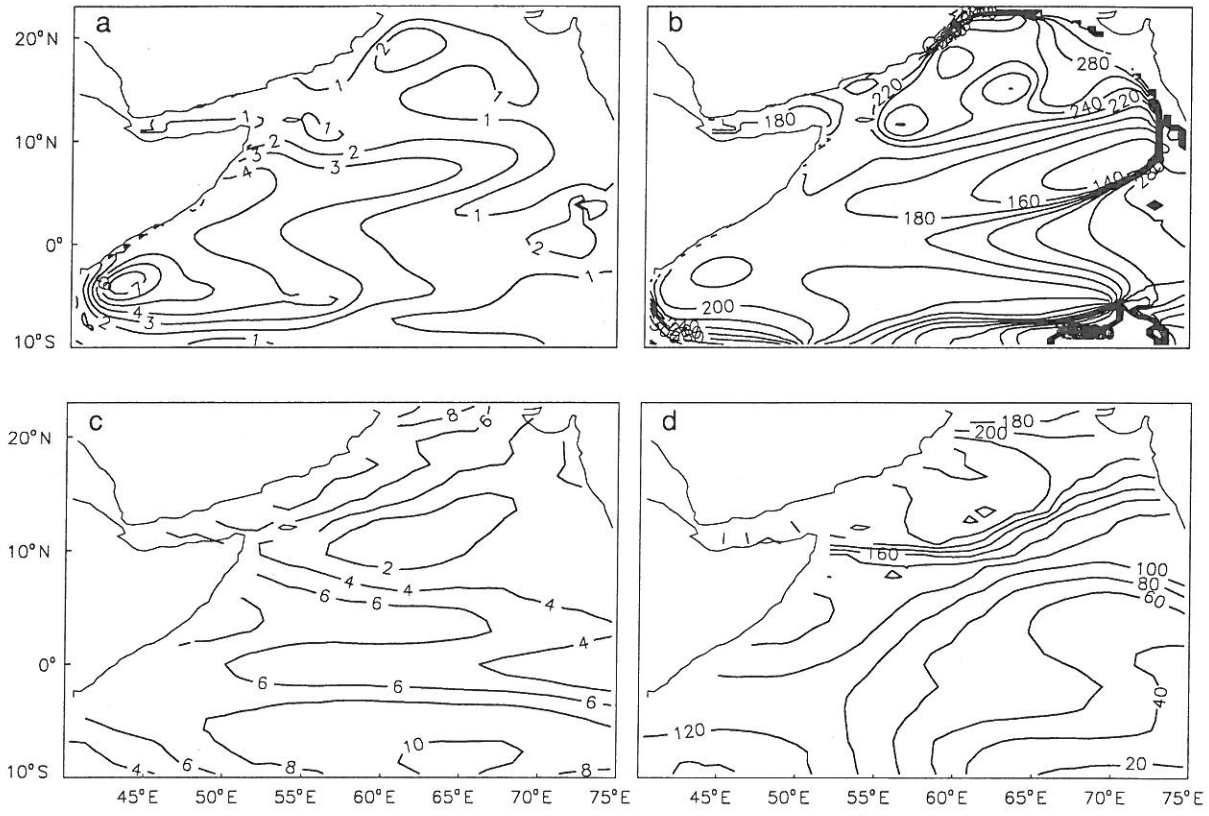

Figure 13. Spatial patterns of the second CEOF eigenvector for the sea level anomaly. (a) Model Amplitude, (b) Model Phase, (c) TP Amplitude, and (d) TP Phase.)

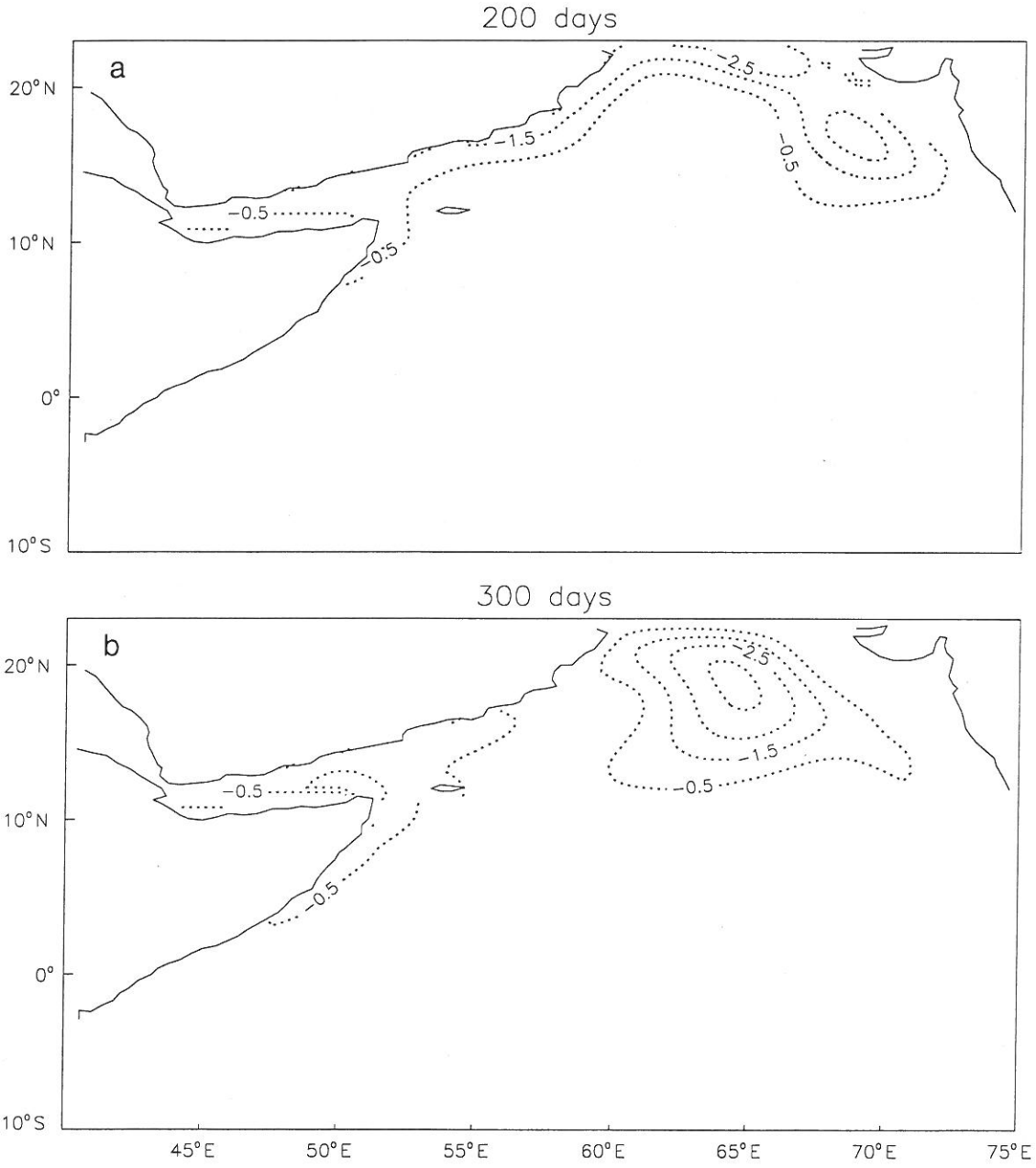

Figure 14. The difference in sea level simulated by the full and partially damped (at the eastern boundary)versions of the model after (a) 200 days, and (b) 300 days.